MNRAS **000**, 1–12 (2002) Preprint 1 December 2016 Compiled using MNRAS LATEX style file v3.0

On the radial profile of gas-phase Fe/α ratio around distant galaxies

Fakhri S. Zahedy[1⋆], Hsiao-Wen Chen[1,2†], Jean-René Gauthier[3], Michael Rauch[4]
[1] *Department of Astronomy & Astrophysics, The University of Chicago, Chicago, IL 60637, USA*
[2] *Kavli Institute for Cosmological Physics, The University of Chicago, Chicago, IL 60637, USA*
[3] *DataScience, Inc., Culver City, CA, USA*
[4] *The Observatories of the Carnegie Institution for Science, 813 Santa Barbara Street, Pasadena, CA 91101, USA*

arXiv:1611.09874v1 [astro-ph.GA] 29 Nov 2016

1 December 2016

ABSTRACT

This paper presents a study of the chemical compositions in cool gas around a sample of 27 intermediate-redshift galaxies. The sample comprises 13 massive quiescent galaxies at $z = 0.40 - 0.73$ probed by QSO sightlines at projected distances $d = 3 - 400$ kpc, and 14 star-forming galaxies at $z = 0.10 - 1.24$ probed by QSO sightlines at $d = 8 - 163$ kpc. The main goal of this study is to examine the radial profiles of the gas-phase Fe/α ratio in galaxy halos based on the observed Fe II to Mg II column density ratios. Because Mg^+ and Fe^+ share similar ionization potentials, the relative ionization correction is small in moderately ionized gas and the observed ionic abundance ratio $N(\mathrm{Fe\,II})/N(\mathrm{Mg\,II})$ places a lower limit to the underlying (Fe/Mg) elemental abundance ratio. For quiescent galaxies, a median and dispersion of $\log\langle N(\mathrm{Fe\,II})/N(\mathrm{Mg\,II})\rangle_{\rm med} = -0.06 \pm 0.15$ is found at $d \lesssim 60$ kpc, which declines to $\log\langle N(\mathrm{Fe\,II})/N(\mathrm{Mg\,II})\rangle_{\rm med} < -0.3$ at $d \gtrsim 100$ kpc. On the other hand, star-forming galaxies exhibit $\log\langle N(\mathrm{Fe\,II})/N(\mathrm{Mg\,II})\rangle = -0.25 \pm 0.21$ at $d \lesssim 60$ kpc and $\log\langle N(\mathrm{Fe\,II})/N(\mathrm{Mg\,II})\rangle = -0.9 \pm 0.4$ at larger distances. Including possible differential dust depletion or ionization correction would only increase the inferred (Fe/Mg) ratio. The observed $N(\mathrm{Fe\,II})/N(\mathrm{Mg\,II})$ implies super-solar Fe/α ratios in the inner halo of quiescent galaxies. An enhanced Fe abundance indicates a substantial contribution by Type Ia supernovae in the chemical enrichment, which is at least comparable to what is observed in the solar neighborhood or in intracluster media but differs from young star-forming regions. In the outer halos of quiescent galaxies and in halos around star-forming galaxy, however, the observed $N(\mathrm{Fe\,II})/N(\mathrm{Mg\,II})$ is consistent with an α-element enhanced enrichment pattern, suggesting a core-collapse supernovae dominated enrichment history.

Key words: galaxies:haloes – galaxies:elliptical and lenticular, cD – quasars:absorption lines – galaxies: abundances

1 INTRODUCTION

The presence of chemically-enriched gas out to large projected distances $d \sim 100$ kpc from galaxies is commonly attributed to super-galactic winds in starburst galaxies (e.g., Murray et al. 2011; Booth et al. 2013, Borthakur et al. 2013). However, the presence of chemically-enriched cool gas around quiescent galaxies both in the local universe and at high redshifts (e.g., Young et al. 2011; Gauthier & Chen 2011; Zhu et al. 2014; Huang et al. 2016) is difficult to reconcile on the basis of a simple outflow model. Because of a lack of intense star formation for $\gtrsim 1$ Gyrs in these quiescent galaxies, additional mechanisms beyond super-galactic winds are clearly needed to explain the presence of chemically enriched gas around galaxies. While tidal interactions and ram pressure force can work to remove interstellar gas of satellite galaxies and fill the halo around the primary galaxy (e.g., Wang 1993; Agertz et al. 2009; Gauthier 2013), without a continuing feedback mechanism the gas is expected to cool and trigger new generations of star formation in the center of the galaxy (e.g., Conroy et al. 2015).

In a recent study, Zahedy et al. (2016) investigated the cool gas content around three lensing galaxies at redshift

⋆ E-mail: fsz@uchicago.edu
† E-mail: hchen@oddjob.uchicago.edu

© 2002 The Authors

$z \sim 0.5$, using multiply-lensed QSOs. These lensing galaxies are massive with total stellar mass of $\log M_*/M_\odot \gtrsim 11$ and half-light radii of $r_e = 2.6-8$ kpc. Their spectral and photometric properties resemble nearby elliptical galaxies, showing no trace of on-going star formation. The multiply-lensed images of the background QSOs occur at $d = 3-15$ kpc, corresponding to $1-2\,r_e$, and therefore provide a sensitive probe of both interstellar and circumgalactic gas in these quiescent, lensing galaxies. An interesting finding from this study is that wherever Mg II absorption transitions are detected, strong Fe II absorption features are also found with an observed column density ratio, $N(\mathrm{Fe\,II})/N(\mathrm{Mg\,II})$, exceeding the typical values seen along random QSO sightlines (e.g., Rigby et al. 2002; Narayanan et al. 2008). In addition, the absorption profiles reveal complex gas kinematics with 8−15 individual components per sightline over a line-of-sight velocity interval of $\Delta\,v \approx 300-600$ km s^{-1}.

The observed relative abundance of singly-ionized iron and magnesium has two important utilities. First of all, because Mg^+ and Fe^+ share similar ionization potentials, the relative ionization correction is small in moderately ionized gas. As demonstrated in Zahedy et al. 2016, in most conditions the observed ionic column density ratio $N(\mathrm{Fe\,II})/N(\mathrm{Mg\,II})$ places a lower limit on the underlying (Fe/Mg) elemental abundance ratio. Secondly, while iron is produced in both core collapse and Type Ia supernovae (SNe) (e.g., Tsujimoto et al. 1995), magnesium is an α element produced primarily in massive stars and core-collapse SNe (e.g., Nomoto et al. 2006). The lower limit of the underlying Fe/Mg elemental abundance ratio from the observed $N(\mathrm{Fe\,II})/N(\mathrm{Mg\,II})$ therefore provides a powerful means of distinguishing between different chemical enrichment sources. Zahedy et al. (2016) found that the cool gas in the vicinities of massive lensing galaxies exhibits a uniformly super-solar (Fe/Mg) abundance pattern, and concluded that the Fe-rich gas is most likely located in the interstellar medium (ISM) of the lensing galaxies with a significant contribution ($\gtrsim 20\%$) of Type Ia supernovae (SNe Ia) to the ISM chemical enrichment history.

The findings of Zahedy et al. (2016) illustrate the potential of applying the observed $N(\mathrm{Fe\,II})/N(\mathrm{Mg\,II})$ to gain new insights into the origin of chemically-enriched diffuse gas around distant galaxies. Specifically, recently accreted gas from the intergalactic medium (IGM) is expected to show α-element enhanced abundance pattern, reflecting its early enrichment history (e.g., Rauch et al. 1997), while stripped gas from the ISM of evolved satellites is expected to display a relatively more Fe-rich pattern owing to a longer lifetime over which more SNe Ia can occur and contribute a higher fraction of Fe-peak elements to the environment.

On the other hand, the Zahedy et al. (2016) study also raises an interesting question regarding the extent of SNe Ia-dominated feedback in quiescent galaxies. It has been found that the radial distribution of the rate of Type Ia SNe in early-type galaxies appears to follow the same Sérsic profile describing the stellar light distribution of the galaxies (Förster & Schawinski 2008). If cool gas around passive galaxies is locally enriched by SNe Ia, then a radial dependence in Fe/α should be expected, with a higher fraction of Fe-rich absorbers observed at smaller d. In this paper, we expand the lensing sample studied in Zahedy et al. (2016), which probes the ISM of massive quiescent galaxies at $d < 15$ kpc, to include both quiescent and star-forming galaxies with measurements of $N(\mathrm{Fe\,II})$ and $N(\mathrm{Mg\,II})$ available out to $z \approx 200$ kpc. This expanded sample allows us to examine the radial profiles of the gas-phase Fe/α ratio in galaxy halos based on the observed $N(\mathrm{Fe\,II})/N(\mathrm{Mg\,II})$.

This paper is organized as follows. Section 2 presents the QSO-galaxy pair sample, as well as the QSO spectroscopic data and corresponding data reduction. The absorption-line measurements are presented in Section 3, and the observed absorption-line properties as a function of projected distance from passive and star-forming galaxies are presented in Section 4. Finally, a discussion of the implications is presented in Section 5. Throughout this paper, a Λ cosmology of $\Omega_\mathrm{M} = 0.3$ and $\Omega_\Lambda = 0.7$, with a Hubble constant of $H_0 = 70$ km s^{-1} Mpc^{-1} is adopted.

2 OBSERVATIONAL DATA

A sample of 27 intermediate-redshift galaxies is assembled for investigating the radial profiles of the gas-phase Fe/α ratio in galaxy halos. This galaxy sample comprises 13 passive galaxies at $z = 0.40-0.73$ and 14 star-forming galaxies at $z = 0.10-1.24$ from a combination of a literature search and our own observations. These galaxies are probed by background QSO sightlines over a range of projected distances, from $d \approx 3$ kpc to $d \approx 400$ kpc for the subsample of passive galaxies and from $d \approx 8$ kpc to $d \approx 160$ kpc for the subsample of star-forming galaxies. Here we describe the assembly of the galaxy sample, and associated echelle spectroscopy of the background QSOs.

2.1 Absorbing Galaxy Sample

We first performed a literature search of intermediate-redshift galaxies that are associated with known Mg II absorbers and have high-resolution echelle absorption spectra of the background QSOs available in the public data archives. Our search resulted in 16 Mg II absorbing galaxies at redshifts $0.10 \leqslant z \leqslant 0.95$ in 10 QSO fields: PKS 0122−0021, PKS 0349−1438, PKS 0439−433, PKS 0454−2203, Q1148+387, Q1241+176, PKS 1354+1933, PKS 1424−1150, 3C 336, and Q2206−199. A number of studies have previously investigated the photometric and spectroscopic properties of these absorbing galaxies (e.g, Steidel et al. 1997, 2002; Chen et al. 1998, 2001, 2005, 2008; Kacprzak et al. 2010, 2011), based on high-resolution *Hubble Space Telescope* (*HST*) imaging and deep ground-based spectroscopic observations. We utilized these studies to classify the selected galaxies into two subsamples: star-forming and passive galaxies. Star-forming galaxies are classified based on an emission-line dominated spectrum or a disk-dominated light profile (disk-to-bulge light ratios > 3, e.g., Chen et al. 1998) when the galaxy spectrum is not available. Passive galaxies are classified based on an absorption-line dominated spectrum and a bulge-dominated light profile (disk-to-bulge light ratios of < 3). Following these criteria, 13 galaxies are classified as star-forming galaxies, whereas 3 galaxies are classified as passive galaxies. In addition to these previously known Mg II-absorbing galaxies, we included a

Table 1. Summary of galaxy and absorption properties

QSO Sightline	Galaxy						Absorption[a]				
	RA (J2000)	Dec (J2000)	$z_{\rm gal}$	Ref.[b]	L_B/L_*	d (kpc)	$W_r(2796)$ (Å)	log N_{tot}(Fe II)[c]	log N_{tot}(Mg II)[d]	log N_{tot}(Mg I)[c]	log $\langle\frac{N(\rm Fe\,II)}{N(\rm Mg\,II)}\rangle$
(1)	(2)	(3)	(4)	(5)	(6)	(7)	(8)	(9)	(10)	(11)	(12)
Passive galaxies											
HE 0047−1756 *A*	00:50:27.84	−17:40:09.6	0.408	Z16	0.9	5	4.46 ± 0.02	14.61	14.67	12.97	-0.06 ± 0.14
HE 0047−1756 *B*						3	3.69 ± 0.04	14.70	14.98	12.86	-0.28 ± 0.16
SDSSJ1025+0349	10:25:32.53	+03:49:25.0	0.4650	BOSS	1.7	166	2.38 ± 0.03	14.45	> 14.48	12.41	< -0.03
HE 1104−1805 *A*	11:06:33.45	−18:21:24.5	0.729	L00	3.5	8	0.64 ± 0.01	13.50	13.44	11.75	0.06 ± 0.04
SDSSJ1144+0714	11:44:45.30	+07:14:56.5	0.4906	GC11	2.1	100	0.74 ± 0.01	14.03	14.72	12.41	-0.69 ± 0.16
SDSSJ1146+0207	11:46:58.64	+02:07:16.8	0.5437	GC11	2.6	74	1.48 ± 0.05	14.45	> 14.23	12.34	< 0.22
Q1241+176[e]	12:44:09.17	+17:21:11.9	0.5591	BOSS	3.8	159	0.14 ± 0.01	< 11.80	12.50	< 10.61	< -0.70
	12:44:11.05	+17:21:04.9	0.5507	CSV96	0.5	21	0.48 ± 0.01	13.68	13.68	12.00	0.00 ± 0.05
SDSSJ1422+0414	14:22:42.63	+04:15:12.0	0.5512	GC11	2.6	211	0.28 ± 0.01	13.13	13.71	11.07	-0.58 ± 0.04
SDSSJ1506+0419	15:06:38.26	+04:19:06.9	0.6155	GC11	3.4	299	0.35 ± 0.02	13.23	13.69	< 11.28	-0.46 ± 0.08
3C 336	16:24:37.52	+23:45:06.0	0.3675	S97	1.2	113	0.25 ± 0.01	12.99	13.11	11.13	-0.12 ± 0.22
	16:24:38.59	+23:45:21.9	0.3181	S97	0.6	55	0.51 ± 0.01	13.39	13.66	11.33	-0.27 ± 0.19
SDSSJ2116−0624	21:16:25.96	−06:24:15.4	0.5237	GC11	2.3	144	0.55 ± 0.01	13.45	> 13.80	11.66	< -0.35
SDSSJ2324−0951	23:24:50.18	−09:50:48.5	0.5446	GC11	2.1	398	1.65 ± 0.03	13.79	> 14.12	12.28	< -0.33
Star-forming galaxies											
PKS 0122−0021	01:25:27.67	−00:05:31.4	0.3985	M15	1.8	163	0.34 ± 0.02	12.74	14.29	11.92	-1.55 ± 0.28
	01:25:28.21	−00:05:54.6	0.9541	M15	1.6	77	0.12 ± 0.01	12.00	12.91	< 10.89	-0.91 ± 0.12
PKS 0349−1438	03:51:27.80	−14:28:58.2	0.3567	C98	0.6	72	0.21 ± 0.01	13.07	13.97	11.04	-0.91 ± 0.11
PKS 0439−433	04:41:17.25	−43:13:40.1	0.1010	CKR05	1.0	8	...	14.92	15.51[f]	...	-0.59 ± 0.07[h]
PKS 0454−2203	04:56:08.82	−21:59:27.0	0.4838	K10	1.4	108	0.42 ± 0.01	13.49	13.66	11.83	-0.17 ± 0.08
Q 1148+387[e]	11:51:29.26	+38:25:56.4	0.5536	S02	1.0	23	0.64 ± 0.01	13.49	13.74	< 11.08	-0.25 ± 0.05
PKS 1354+1933	13:57:04.53	+19:19:15.1	0.4592	EGY91	0.5	44	0.85 ± 0.01	13.64	13.88	11.86	-0.24 ± 0.14
PKS 1424−1150	14:27:38.18	−12:03:32.9	0.3404	C01	0.6	85	0.15 ± 0.02	< 12.73	12.70	11.49	< 0.03
SDSSJ1430+0149	14:30:40.71	+01:49:40.8	1.2418	Z16b	0.8	17	2.86 ± 0.01	15.23	15.48[g]	13.04	-0.25 ± 0.09[i]
3C 336	16:24:38.19	+23:45:22.0	0.702	S97	0.5	113	0.040 ± 0.003	< 11.35	12.16	< 10.25	< -0.81
	16:24:38.42	+23:45:15.2	0.798	S97	0.4	71	0.45 ± 0.01	12.59	13.29	< 11.02	-0.70 ± 0.08
	16:24:38.77	+23:45:08.3	0.472	S97	0.2	34	0.81 ± 0.01	13.52	14.12	11.70	-0.59 ± 0.12
	16:24:39.30	+23:45:12.1	0.892	S97	0.7	23	1.55 ± 0.01	14.73	> 14.50	12.50	< 0.23
Q2206−199	22:08:51.55	−19:43:52.6	0.948	GB97	2.1	87	0.25 ± 0.01	12.48	13.37	10.87	-0.89 ± 0.15

Notes

[a] The typical uncertainty in total column densities of Fe II, Mg II, and Mg I absorption (Columns 9 through 11) is smaller than 0.05 dex for all absorption systems; see § 3. The quoted uncertainty in $\log\langle N(\rm Fe\,II)/N(\rm Mg\,II)\rangle$ (Column 12) for each system is the dispersion from the weighted mean, which represents the scatter in $N(\rm Fe\,II)/N(\rm Mg\,II)$ among individual components of the corresponding absorber.

[b] References for galaxy redshifts: Ellingson, Green & Yee 1991 (EGY91); Churchill, Steidel & Vogt 1996 (CSV96); Steidel et al. 1997 (S97); Guillemin & Bergeron 1997 (GB97); Chen et al. 1998 (C98); Lidman et al. 2000 (L00); Chen et al. 2001 (C01); Steidel et al. 2002 (S02); Chen, Kennicutt & Rauch 2005 (CKR05); Kacprzak et al. 2010 (K10); Gauthier & Chen 2011 (GC11); Dawson et al. 2013 (BOSS); Muzahid et al. 2015 (M15); Zahedy et al. 2016 (Z16); This work (Z16b).

[c] The upper limits are 2-σ limits on the total column density for non detections, estimated using the error spectrum.

[d] The lower limits represent 2-σ limits on the total column density for saturated Mg II $\lambda\lambda$ 2796, 2803 absorption doublet.

[e] Absorption-line measurements for these fields are adopted from Churchill et al. (2000) and Churchill & Vogt (2001).

[f] Because the Mg II $\lambda\lambda$ 2796, 2803 absorption doublet falls outside the observable spectral window for this QSO sightline, the total N(Mg II) of the system was estimated from the total S II column density of the system, $\log N_{\rm tot}$(S II); see § 3.

[g] Because the Mg II $\lambda\lambda$ 2796, 2803 absorption doublet is heavily saturated for this absorption system, $\log N_{\rm tot}$(Mg II) was estimated from the total Si II column density of this system, $\log N_{\rm tot}$(Si II); see § 3.

[h] The error is estimated by propagating the statistical errors for $\log N_{tot}$ (Fe,II), $\log N_{tot}$(S II), and the uncertainty in the adopted (Mg/S) ratio from Asplund et al. 2009; see § 3.

[i] The error is estimated by propagating the statistical errors for $\log N_{tot}$ (Fe,II), $\log N_{tot}$(Si II), and the uncertainty in the adopted (Mg/Si) ratio from Asplund et al. 2009; see § 3.

newly identified $z_{\rm gal} = 1.2418$ star-forming galaxy at $d = 17$ kpc from the QSO SDSSJ 1430+0149, where an ultra-strong Mg II absorber of rest-frame absorption equivalent width $W_r(2796) \approx 2.8$ Å had been identified at the same redshift (e.g., Zych et al. 2009).

To increase the number of passive galaxies in our sample, we included Luminous Red Galaxies (LRGs) at $z \sim 0.5$ with associated Mg II absorption features from Gauthier & Chen (2011). We further supplemented this passive galaxy subsample with new, unpublished Mg II-absorbing LRGs from our own survey. Together with two massive lensing galaxies with associated Mg II absorption from Zahedy et al. (2016), this process resulted in 10 additional passive galaxies probed by 11 QSO sightlines at $d = 3 - 398$ kpc. A summary of the properties of the final sample of 27 galaxies is presented in Columns 2 to 7 of Table 1, where we list for each galaxy its right ascension and declination, redshift $z_{\rm gal}$, galaxy projected distance from the QSO sightline d, and the B-band luminosity L_B in unit of L_*, calculated using the redshift-dependent absolute B-band magnitude measurements from Faber et al. (2007).

2.2 QSO Absorption Spectroscopy

High-resolution echelle spectra of the QSOs PKS 0349−1438, PKS 1424−1150, SDSS J1430+0149, 3C336, and Q2206−199 were obtained using the Ultraviolet and Visual Echelle Spectrograph (UVES; D'Odorico et al. 2000) on the VLT-UT2 telescope under multiple observing programs (PIDs 076.A-0860(A), 075.A-0841(A), 079.A-0656(A), 081.A-0478(A), 69.A-0371(A), and 65.O-0158(A), respectively). We retrieved the reduced and order-combined individual exposures from the ESO Advanced Data Products Archive. Following data retrieval, we performed vacuum and heliocentric corrections to the QSO spectra, co-added different exposures, and performed continuum fitting to the data. The resulting spectra typically have a high signal-to-noise ratio of $S/N > 15$ per resolution element of $7 - 8$ km s^{-1} in full-width-at-half-maximum (FWHM).

Echelle spectroscopic observations were obtained using the MIKE echelle spectrograph (Bernstein et al. 2003) on the Magellan Clay Telescope for the QSOs PKS 0122−0021, PKS 0349−1438, PKS 0454−2203, SDSSJ1144+0714, SDSSJ1422+0414, SDSSJ1506+0419, SDSSJ1025+0349, SDSSJ1146+0207, SDSSJ2116−0624, and SDSSJ2324−0951 during multiple observing runs

Table 2. Journal of QSO echelle spectroscopy

QSO Image (1)	$z_{\rm em}$ (2)	Instrument (3)	Exp. time (s) (4)	Date (5)
3C336	0.927	UVES	9800	2002 Apr, May
HE 0047−1756*A*	1.676	MIKE	7200	2013 Nov
HE 0047−1756*B*	1.676	MIKE	5700	2013 Nov
HE 1104−1805*A*	2.305	HIRES	19300	1997 Feb
		UVES	19000	2001 Jun
PKS 0122−0021	1.077	MIKE	1200	2007 Oct
PKS 0349−1438	0.616	MIKE	1800	2007 Oct
PKS 0454−2203	0.533	MIKE	2700	2007 Oct
PKS 1354+1933	0.720	UVES	600	2001 Jun
PKS 1424−1150	0.806	UVES	720	2005 Jul
Q2206−199	2.558	UVES	17100	2000 May
SDSSJ1025+0349	1.325	MIKE	5400	2015 Apr
SDSSJ1144+0714	0.919	MIKE	6000	2010 May
SDSSJ1146+0207	1.137	MIKE	9000	2010 May
SDSSJ1422+0414	0.972	MIKE	6000	2010 May
SDSSJ1430+0149	2.119	UVES	12150	2007 May, Jun
		UVES	2930	2008 Aug
SDSSJ1506+0419	1.288	MIKE	9000	2010 May
SDSSJ2116−0624	1.042	MIKE	8000	2010 May
SDSSJ2324−0951	0.764	MIKE	9000	2010 Sep

between October 2007 and April 2015. A 1″ slit and 2 × 2 binning were employed for the observations of PKS 0122−0021, PKS 0349−1438, PKS 0454−2203, SDSSJ1144+0714, SDSSJ1422+0414, SDSSJ1506+0419, SDSSJ2116−0624, and SDSSJ2324−0951. A 0.7″ slit and 2 × 2 binning were employed for the observations of SDSSJ1146+0207, and a 0.7″ slit and 3 × 3 binning were employed for the observations of SDSSJ1025+0349. MIKE delivers spectral resolutions of FWHM ∼ 12 km s^{-1} and 8 km s^{-1} for the 1.0″ and 0.7″ slits, respectively. The spectra were reduced using a custom data reduction pipeline previously described in Chen et al. (2014) and Zahedy et al. (2016). The final combined spectra are characterized by $S/N > 10$ per resolution element at $\lambda > 3500$ Å. Finally, details of the data reduction for the echelle spectra of the two lensed QSO systems HE 0047−1756 (MIKE) and HE 1104−1805 (UVES and Keck HIRES) have previously been described in Zahedy et al. (2016). A journal of the echelle spectroscopic observations of the QSO sightlines in our study is shown in Table 2.

3 ABSORPTION LINE ANALYSIS

The high-resolution echelle spectra of the QSOs described in § 2 enable accurate constraints on both the integrated rest-frame Mg II absorption equivalent width ($W_r(2796)$) and the ionic column densities of Fe^+, Mg^+, and Mg^0 for each galaxy in our sample. In particular, a component-by-component analysis allows us to examine how the relative abundance ratios between any two ions vary within individual galaxy halos and across the full sample (e.g., Zahedy et al. 2016). We employ a custom software, previously developed by and described in Zahedy et al. (2016), to perform a Voigt profile fitting analysis for constraining the Mg II, Mg I, and Fe II column densities of individual absorbing components. We perform a simultaneous fit to prominent absorption transitions, including the Mg II λλ 2796, 2803 doublet, Mg I λ 2852, and a series of Fe II transitions. For all galaxies, Fe II λ 2600 and Fe II λ 2586 transitions are included in the Voigt profile analysis. For galaxies at $z \gtrsim 0.5$, additional Fe II λ 2382, Fe II λ 2374, and Fe II λ 2344 transitions are included.

For individual Mg II absorbing components with no corresponding Fe II or Mg I absorption, we measure a 2-σ upper limit in the absorption equivalent width of the strongest transitions using the error spectrum. The upper limits are evaluated over a spectral window twice the FWHM of the corresponding Mg II component. The measured 2-σ equivalent width limits are then converted to 2-σ upper limits of the component column densities under an optically-thin assumption. For saturated Mg II absorbing components, we place 2-σ lower limits of the component column densities based on a grid search of the χ^2 values from the Voigt profile fitting results.

In five cases, we cannot measure the Mg II absorption strength directly either due to missing echelle spectra in the public archives or a lack of spectral coverage for the relevant transitions. Three of these systems are identified along QSO sightlines Q1241+176 and Q1148+387. The observed $W_r(2796)$ and total Fe II, Mg II, and Mg I column density measurements for these systems have been published in Churchill et al. (2000) and Churchill & Vogt (2001). We adopt these values for our subsequent analysis. In addition, the galaxy at $z = 0.101$ in the field of PKS 0439−433 does not have Mg II absorption spectra available. The Mg II absorber associated with the galaxy at $z = 1.24$ in the field of SDSSJ 1430+0549 is heavily saturated, and no useful constraint for the Mg II absorption column density is available. Finally, two lensing galaxies have been published in Zahedy et al. (2016). Excluding these galaxies leads to 20 galaxies for which we can perform our own Voigt profile analysis. The results of the component-by-component Voigt profile analysis of Mg II, Mg I, and Fe II absorption for these 20 galaxies are presented in Figure 1.

For the galaxy at $z = 0.101$ and $d = 8$ kpc from PKS 0439−433, a damped Lyman Lyα (DLA) absorption feature is found in the QSO spectrum. Measurement of the total Fe II column density, $N_{\rm tot}$(Fe II), is based on far-ultraviolet transitions observed using the Cosmic Origins Spectrograph (COS; Green et al. 2012) on board *HST*. We adopt $\log N_{\rm tot}$(Fe II)$= 14.92 \pm 0.03$ from Som et al. (2015). Furthermore, because no Mg II column density measurement is available for this galaxy, we infer the total Mg II column density, $N_{\rm tot}$(Mg II), from the reported total column density of another α-element ion S^+, $N_{\rm tot}$(S II). For this DLA, Som et al. (2015) measured $\log N_{\rm tot}$(S II)$= 15.03 \pm 0.03$. We assume a solar elemental abundance pattern of $\log (\rm Mg/S)_\odot = 0.5$ dex (Asplund et al. 2009) for this system, motivated by the observed near-solar metallicity of the DLA (e.g., Chen et al. 2005; Som et al. 2015). To investigate the ionization correction between the elemental ratio (Mg/S) and the observed ionic ratio $N_{\rm tot}$(Mg II)/$N_{\rm tot}$(S II), we perform photoionization calculations using Cloudy (Ferland et al. 2013; v.13.03) for a $T = 10^4$ K cloud with neutral hydrogen column density and metallicity reported for this system ($\log N$(H I) = 19.63; [S/H]= 0.1). We assume a plane-parallel geometry for the gas cloud, which is illuminated on both sides with an updated Haardt & Madau (2001) ionizing radiation field (HM05 in Cloudy) at $z = 0.1$. Using the photoionization model and applying $N_{\rm tot}$(Fe II)/$N_{\rm tot}$(Fe III) of the absorbing gas for constraining the mean ionization parameter, we find that the ionization correction is negligible

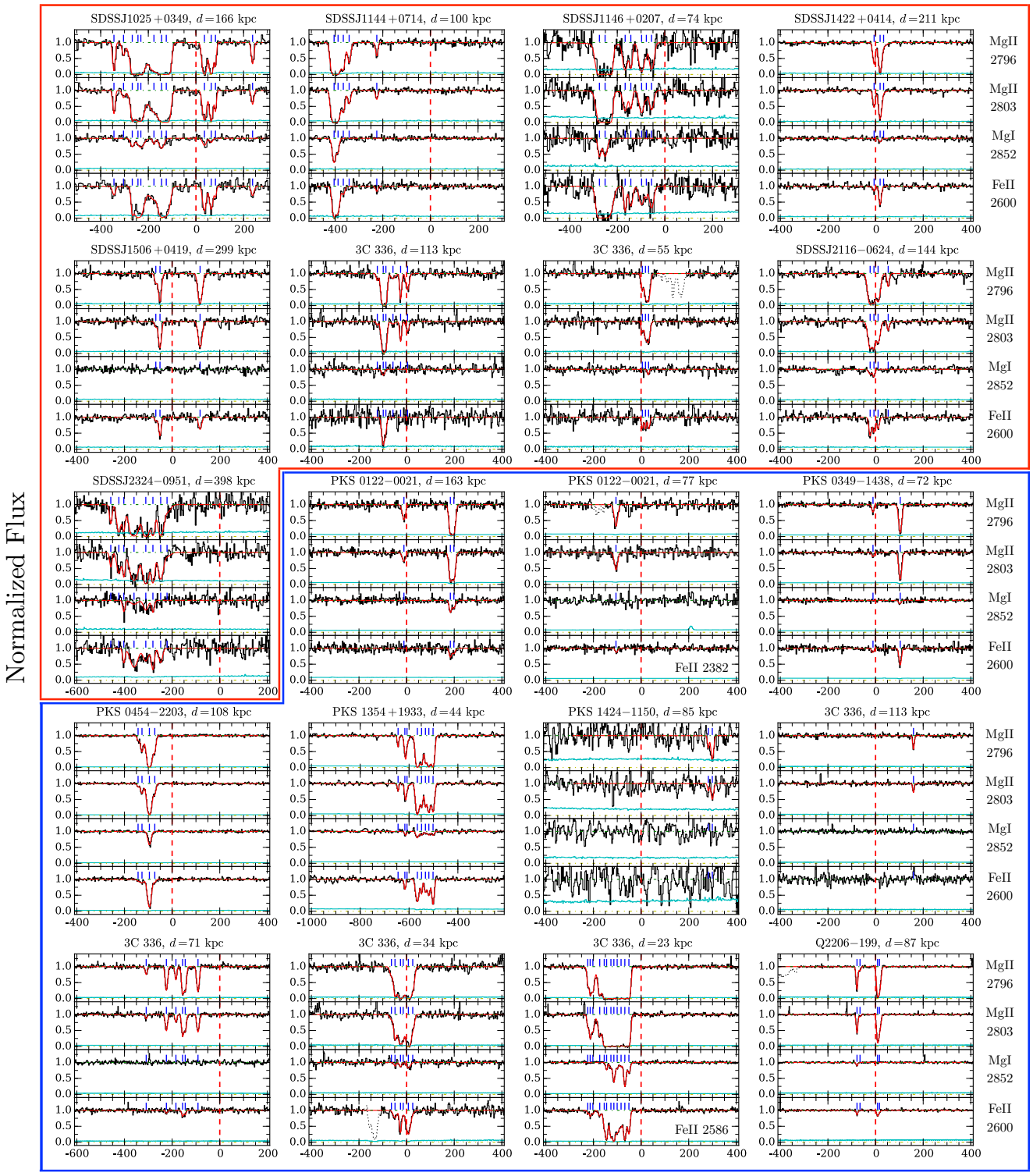

Figure 1. Summary of the component-by-component Voigt profile analysis of Mg II, Mg I, and Fe II absorption for 20 galaxies that have not been published previously. For each galaxy, the observed absorption files of the Mg II doublet, Mg I λ 2852, and Fe II λ 2600 are presented from top to bottom panels. In each panel, the absorption spectra and corresponding 1-σ error array are shown in black and cyan, respectively. The best-fit Voigt profile is shown in red. Contaminating features have been dotted out for clarity. The centroid of each absorbing component is marked by a blue tick mark at the top of each panel. Zero velocity corresponds to the systemic redshift of the absorbing galaxy. Galaxy projected distance is indicated at the top of each four-panel block. Finally, the red outlining box encloses passive galaxies and blue includes star-forming galaxies.

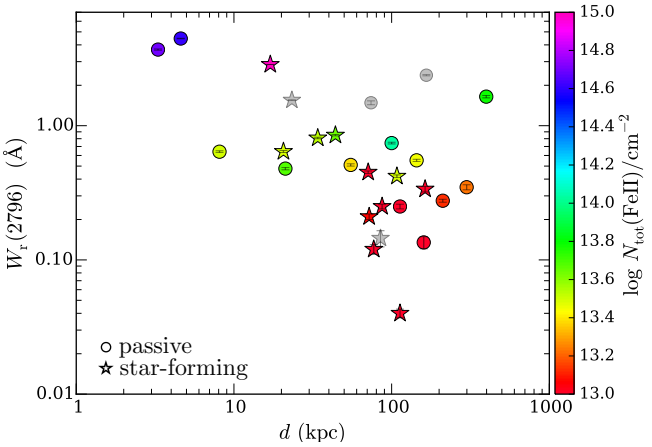

Figure 2. Rest-frame Mg II absorption equivalent width $W_r(2796)$ versus galaxy projected distance d for the galaxy sample in this study. Circles represent passive galaxies, while stars represent star-forming galaxies. The color of each data point represents the total Fe II column density, $\log N_{\rm tot}$(Fe II) of the absorption system associated with each galaxy. Greyed out data points mark absorption systems with no constraints on the mean Fe II/Mg II ratio (see Figure 4 below) due to saturation (three galaxies) and poor signal-to-noise ratio (one galaxy). We note that the Mg II doublet falls outside the observable window for PKS 0439−433 and thus is not plotted here (see also § 3 for a detailed discussion on this system).

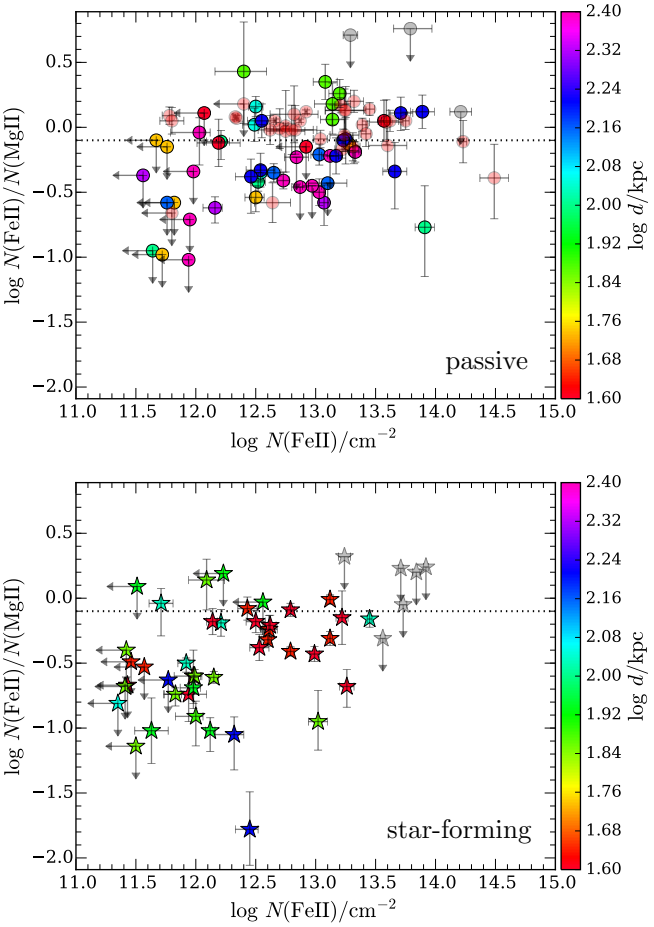

Figure 3. Observed Fe II to Mg II column density ratios versus Fe II column density for individual components associated with passive (circles in the top panel) and star-forming (star symbols in the bottom panel) galaxies in this study. Error bars associated with each data point show the measurement uncertainties. The color of each data point represents the projected distance d of the absorbing galaxy. Saturated components associated with galaxies with poor constraints on the mean Fe II/Mg II ratio (see Figure 4 below) are greyed out. Both lensing galaxies in the passive subsample exhibit strong Mg II absorption at $d < 10$ kpc. The absorbers are resolved into $8-15$ components and show pre-dominantly Fe-rich gas (Zahedy et al. 2016). Components associated with these lensing galaxies are shown in pale red to be separated from non-lensing galaxies at $d > 10$ kpc in the top panel. In both panels, when a Mg II absorbing component has no corresponding Fe II absorption detected, it is shown as downward and left-pointing arrows with the data point indicating the 2-σ upper limit of N(Fe II). In addition, when Mg II components are saturated, the inferred 2-σ lower limit on N(Mg II) directly translates to a 2-σ upper limit on N(Fe II)/N(Mg II). The dotted horizontal line indicates the solar (Fe/Mg) abundance pattern from Asplund et al. (2009), $\log$ (Fe/Mg)$_\odot = -0.10$, to guide visual comparisons.

between (Mg/S) and $N_{\rm tot}$(Mg II)/$N_{\rm tot}$(S II). Based on the assumed (Mg/S)$_\odot$, we infer $\log N_{\rm tot}$(Mg II)$= 15.51 \pm 0.06$, where the error is estimated by propagating the statistical error for $\log N_{\rm tot}$(S II) and the uncertainty in the adopted (Mg/S) ratio from Asplund et al. 2009.

For the galaxy at $z = 1.2418$ and $d = 17$ kpc from SDSSJ1430+0149, the Mg II absorption line is heavily saturated. We infer $N_{\rm tot}$(Mg II) from the absorption strength of the weaker and non-saturated Si II λ1808 transition also recorded in the public UVES spectra. A Voigt profile analysis returns a best-fit integrated $\log N_{\rm tot}$(Si II)$=$ 15.75 ± 0.05, which is consistent with the published value in Zych et al. (2009). We adopt a solar elemental abundance ratio of $\log$ (Mg/Si)$_\odot = 0.1$ dex for this system, which is consistent with what has been observed for a number of $z > 1$ DLAs (e.g., Dessauges-Zavadsky et al. 2006). The ionization correction between (Mg/Si) and ionic ratio $N_{\rm tot}$(Mg II)/$N_{\rm tot}$(Si II) is estimated using a Cloudy photoionization model for a plane-parallel cloud with 0.1 solar metallicity and $\log N$(H I) $= 19.5$, which is illuminated on both sides with the HM05 radiation field at $z = 1.24$. Using the model output and the observed $N_{\rm tot}$(Mg I)/$N_{\rm tot}$(Si II) ratio, we estimate $N_{\rm tot}$(Mg II)/$N_{\rm tot}$(Si II)$= 0.44 \times N$(Mg)/N(Si) for this system and infer $\log N_{\rm tot}$(Mg II)$=$ 15.48 ± 0.07, where the error is estimated by propagating the statistical error for $\log N_{\rm tot}$(Si II) and the uncertainty in the adopted (Mg/Si) ratio from Asplund et al. 2009.

The results of the absorption-line analysis are summarized in Columns 8 through 11 of Table 1, which present $W_r(2796)$ and the total column densities of Fe II, Mg II, and Mg I absorption, $\log N_{\rm tot}$(Fe II), $\log N_{\rm tot}$(Mg II), $\log N_{\rm tot}$(Mg I), summed over all individual components. Upper limits of the total column densities indicate non-detections, whereas lower limits indicate saturated absorption. The typical uncertainty in the total integrated column densities is smaller than 0.05 dex for all absorption systems.

The general absorption properties of the galaxy sample are summarized by the radial profile of Mg II absorption in Figure 2, which displays the observed $W_r(2796)$ versus

projected distance d for all galaxies in the sample where $W_r(2796)$ measurements are available. The data points are color-coded according to $N_{\rm tot}$(Fe II) associated with each galaxy. Absorption systems with poor constraints on the N(Fe II)/N(Mg II) ratio due to either saturation or low signal-to-noise ratios are shown in gray (see below). With the exception of two passive galaxies at $d > 100$ kpc which exhibit saturated Mg II absorption features, the Mg II absorbing gas around the galaxies in our sample follow a similar declining trend of $W_r(2796)$ with increasing d as presented in Chen et al. (2010) and Nielsen et al. (2013). In addition, the observed N(Fe II) also appears to decline with increasing d.

To examine the relative Fe to Mg abundance pattern, we present in Figure 3 the Fe II to Mg II column density ratio, N(Fe II)/N(Mg II), versus Fe II column density, N(Fe II), for individual absorbing components associated with passive (circles in the top panel) and star-forming (star symbols in the bottom panel) galaxies. The data points are color-coded by the projected distances of the absorbing galaxies, and components associated with the two lensing galaxies (both passive) at $d < 10$ kpc are shown in pale red to be separated from absorbing components found at $d > 10$ kpc from non-lensing galaxies. When Fe II absorption is not detected or when Mg II components are saturated, a 2-σ limit is placed on N(Fe II)/N(Mg II). For heavily saturated Mg II components, no sensitive constraints can be obtained. These components are shown in grey.

Two interesting features are seen in Figure 3. First, passive galaxies (including both lensing and non-lensing galaxies) display a large fraction ($> 50\%$) of Fe II-rich gas at $d < 100$ kpc (data points with colors red through green) with $\log N$(Fe II)/N(Mg II) > -0.1 dex. At larger distances, $d \gtrsim 100$ kpc, only five components associated with two passive galaxies show predominantly Fe II-rich content and the remaining 33 components are consistent with Mg II-rich gas with $\log N$(Fe II)/N(Mg II) $\lesssim -0.1$ dex (data points with colors blue through magenta). Secondly, the majority of absorbing components associated with star-forming galaxies are consistent with an Mg II-rich content with $\log N$(Fe II)/N(Mg II) $\lesssim -0.1$ dex over the full projected distance range probed by the sample. Only three out of 43 non-saturated components display $\log N$(Fe II)/N(Mg II) $\gtrsim -0.1$ dex.

4 THE RADIAL PROFILE OF N(FE II)/N(MG II) IN GALAXY HALOS

Figure 3 suggests that N(Fe II)/N(Mg II) in galaxy halos depends on both the projected distance and star formation history of the absorbing galaxy. To better quantify how the observed N(Fe II)/N(Mg II) ratio depends on galaxy properties, we compute a N(Mg II)-weighted mean Fe II to Mg II column density ratio for each absorption system according to the following equation,

$$\log\left\langle\frac{N(\mathrm{Fe\,II})}{N(\mathrm{Mg\,II})}\right\rangle = \log\sum_i w_i\frac{N_i(\mathrm{Fe\,II})}{N_i(\mathrm{Mg\,II})}$$
$$= \log N_{\rm tot}(\mathrm{Fe\,II}) - \log N_{\rm tot}(\mathrm{Mg\,II}), \quad (1)$$

where $w_i = N_i(\mathrm{Mg\,II})/N_{\rm tot}(\mathrm{Mg\,II})$ for component i, and $\log N_{\rm tot}$(Fe II) and $\log N_{\rm tot}$(Mg II) are the total column densities of Fe II and Mg II, respectively, summed over all individual absorbing components in a given system. The mean N(Fe II)/N(Mg II) ratio for each absorption system is presented in Column 11 of Table 1. The quoted uncertainty in $\log\langle N(\mathrm{Fe\,II})/N(\mathrm{Mg\,II})\rangle$ for each system is the dispersion from the weighted mean, which represents the scatter in Fe II to Mg II column density ratio among individual components of the corresponding absorber.

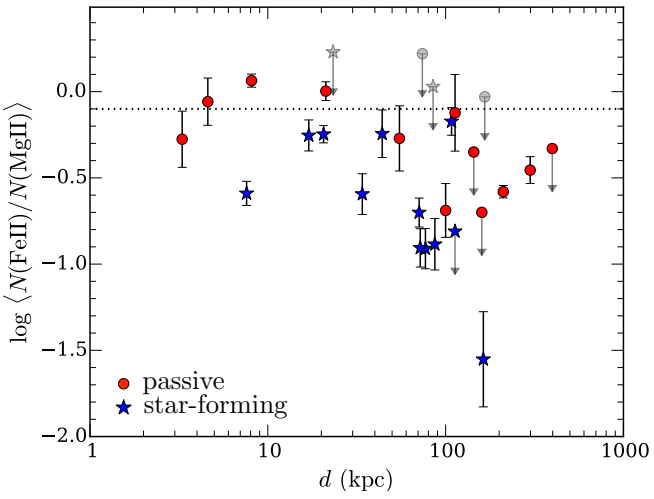

Figure 4. Mean Fe II to Mg II column density ratio, $\langle N(\mathrm{Fe\,II})/N(\mathrm{Mg\,II})\rangle$, from Equation (1) versus galaxy projected distance, d, for absorbers associated with passive galaxies (red circles) and for those associated with star-forming galaxies (blue stars). Error bars for each data point represent the dispersion among individual component Fe II to Mg II ratios of the corresponding absorber. As shown in Figure 3, only 2-σ upper limits can be placed on N(Fe II)/N(Mg II), if Fe II absorption is not detected or if Mg II components are saturated. These upper limits are propagated into the estimates of $\langle N(\mathrm{Fe\,II})/N(\mathrm{Mg\,II})\rangle$ for each absorbing galaxy and are indicated as downward arrows. Four galaxies do not have sensitive constraints for $\langle N(\mathrm{Fe\,II})/N(\mathrm{Mg\,II})\rangle$, either due to heavily saturated Mg II absorbers or absence of a strong limit on the Fe II absorption. These data points are greyed out for clarity. Following Figure 3, the dotted horizontal line indicates the solar (Fe/Mg) abundance pattern, for visual comparisons. Two interesting features are evident: (1) passive galaxies exhibit on average higher $\langle N(\mathrm{Fe\,II})/N(\mathrm{Mg\,II})\rangle$ than star-forming galaxies; and (2) $\langle N(\mathrm{Fe\,II})/N(\mathrm{Mg\,II})\rangle$ appears to show a mild declining trend toward larger d for both passive and star-forming subsamples.

Figure 4 displays $\langle N(\mathrm{Fe\,II})/N(\mathrm{Mg\,II})\rangle$ versus d for passive (red circles) and star-forming (blue stars) galaxies. Three galaxies exhibit heavily saturated Mg II absorbers: (1) the passive galaxy at $z = 0.5437$ and at $d = 74$ kpc from SDSSJ 1146+0207; (2) the passive galaxy at $z = 0.465$ and at $d = 166$ kpc from SDSSJ 1025+0349; and (3) the star-forming galaxy at $z = 0.892$ and at $d = 23$ kpc from 3C336. No meaningful constraints for $\langle N(\mathrm{Fe\,II})/N(\mathrm{Mg\,II})\rangle$ can be obtained for these absorbers. In addition, the star-forming galaxy at $z = 0.3404$ and at $d = 85$ kpc from PKS 1424−1150 exhibit only a weak Mg II absorber and Fe II absorption is not detected. The available absorption spectra do not place a sensitive constraint for $\langle N(\mathrm{Fe\,II})/N(\mathrm{Mg\,II})\rangle$. All four galaxies are greyed out in Figure 4 for clarity. Considering only galaxies for which measurements of (or

strong constraints for) $\langle N(\mathrm{Fe\,II})/N(\mathrm{Mg\,II})\rangle$ are available, it is clear that passive galaxies exhibit on average higher $\langle N(\mathrm{Fe\,II})/N(\mathrm{Mg\,II})\rangle$ than star-forming galaxies. In addition, $\langle N(\mathrm{Fe\,II})/N(\mathrm{Mg\,II})\rangle$ appears to show a mild declining trend toward larger d for both passive and star-forming subsamples.

To further examine the dependence of $N(\mathrm{Fe\,II})/N(\mathrm{Mg\,II})$ ratio on galaxy projected distance d, we divide each of the passive and star-forming subsamples into low- and high-d subsamples. The adopted bin size in d is determined so that there are roughly equal number of galaxies (five to seven galaxies) in each subsample. We then compute the median value $\log\langle N(\mathrm{Fe\,II})/N(\mathrm{Mg\,II})\rangle_{\rm med}$ in each bin as well as the dispersion of each subsample around the median value. Saturated absorption systems are excluded from this exercise, because no constraints on $N(\mathrm{Fe\,II})/N(\mathrm{Mg\,II})$ can be derived either due to heavily saturated Mg II absorption or insufficient limits on $N(\mathrm{Fe\,II})/N(\mathrm{Mg\,II})$ (see Column 12 of Table 1). In addition, for passive galaxies at $d \gtrsim 100$ kpc two of the seven galaxies have only a relatively strong upper limit at $\log\langle N(\mathrm{Fe\,II})/N(\mathrm{Mg\,II})\rangle \approx -0.3$. For this subsample, we infer a 85% upper limit for the underlying distribution of $\log\langle N(\mathrm{Fe\,II})/N(\mathrm{Mg\,II})\rangle_{\rm med} < -0.3$. The results are presented in Figure 5 for passive galaxies (red circles) and star-forming galaxies (blue stars).

Figure 5 shows that $\log\langle N(\mathrm{Fe\,II})/N(\mathrm{Mg\,II})\rangle_{\rm med}$ declines with increasing d, from $\log\langle N(\mathrm{Fe\,II})/N(\mathrm{Mg\,II})\rangle_{\rm med} = -0.06\pm0.15$ at $d < 60$ kpc to $\log\langle N(\mathrm{Fe\,II})/N(\mathrm{Mg\,II})\rangle_{\rm med} < -0.3$ at $d > 100$ kpc. For star-forming galaxies, a similar declining trend is found with increasing d, from $\log\langle N(\mathrm{Fe\,II})/N(\mathrm{Mg\,II})\rangle_{\rm med} = -0.25\pm0.21$ at $d < 44$ kpc to $\log\langle N(\mathrm{Fe\,II})/N(\mathrm{Mg\,II})\rangle_{\rm med} = -0.91\pm0.44$ at $d > 70$ kpc. Furthermore, while $\log\langle N(\mathrm{Fe\,II})/N(\mathrm{Mg\,II})\rangle_{\rm med}$ is about 0.2 dex higher in the inner halos ($d \lesssim 60$ kpc) of passive galaxies than those around star-forming ones, both galaxy populations display a comparable $\log\langle N(\mathrm{Fe\,II})/N(\mathrm{Mg\,II})\rangle_{\rm med}$ in the outer halos.

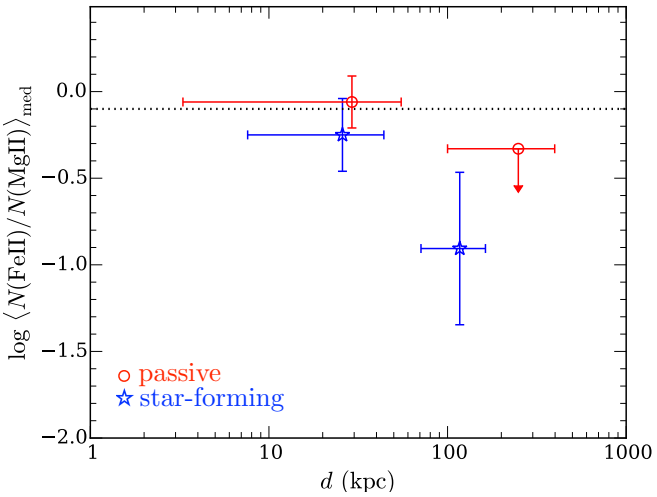

Figure 5. Dependence of median column density ratio, $\log\langle N(\mathrm{Fe\,II})/N(\mathrm{Mg\,II})\rangle_{\rm med}$, on galaxy projected distance d for passive galaxies (red circles) and star-forming galaxies (blue stars). The horizontal error bars represent the full range of projected distances in each bin, whereas the vertical error bars show the dispersion from $\log\langle N(\mathrm{Fe\,II})/N(\mathrm{Mg\,II})\rangle_{\rm med}$ in each bin. Two of the seven passive galaxies at $d \gtrsim 100$ kpc have only a relatively strong upper limit at $\log\langle N(\mathrm{Fe\,II})/N(\mathrm{Mg\,II})\rangle \approx -0.3$ (Figure 4). For this subsample, we infer a 85% upper limit for the underlying distribution of $\log\langle N(\mathrm{Fe\,II})/N(\mathrm{Mg\,II})\rangle_{\rm med} < -0.3$, which is shown as the downward arrow. Like Figure 3, the dotted horizontal line indicates the solar (Fe/Mg) abundance pattern.

5 DISCUSSION

A primary goal of our study is to determine the extent SNe Ia-dominated feedback in gas around galaxies. The analysis presented in §§ 3 & 4 indicate that passive galaxies display on average a higher $N(\mathrm{Fe\,II})/N(\mathrm{Mg\,II})$ in their halos than star-forming galaxies. In addition, there also appears to be a modest decline in the relative ionic ratio with increasing projected distance. To infer the underlying elemental abundance ratio between Fe and Mg from the observed relative abundances of Fe^+ and Mg^+, it is necessary to first address the differential ionization fraction between the two ions. Furthermore, it is also necessary to quantify possible systematic biases due to differential dust depletion. Here we discuss both of these effects and the implications of our findings.

5.1 Differential ionization fraction

To determine the ionization state of the gas, measurements of $N(\mathrm{H\,I})$ and relative abundance ratios between multiple ions are often necessary. While the observed relative ionic ratios constrain the ionization parameters, knowledge of $N(\mathrm{H\,I})$ determines whether the gas is optically-thin or optically-thick to the background radiation field. However, $N(\mathrm{H\,I})$ is not known for all but one galaxy in our sample. As illustrated in Zahedy et al. (2016), useful empirical constraints on the relative Fe/α abundances can be obtained in the absence of $N(\mathrm{H\,I})$. This is achieved by performing a series of photoionization calculations that explore a wide range of ionization conditions. Then, constraints for the ionization state of the gas are obtained based on comparisons of the predicted and observed column density ratios between Mg^0 and Mg^+ ions.

In Figure 6 we present the observed Mg I to Mg II column density ratio, $N(\mathrm{Mg\,I})/N(\mathrm{Mg\,II})$, versus Mg II column density, $N(\mathrm{Mg\,II})$, for individual absorbing components associated with passive (circle symbols) and star-forming (star symbols) galaxies. The data points are color-coded by the projected distances of the absorbing galaxies. Grey data points represent 2-σ upper limit of $N(\mathrm{Mg\,I})/N(\mathrm{Mg\,II})$, due to either non-detection of Mg I or saturated Mg II absorption. Figure 6 shows that the majority ($> 90\%$) of absorbing components with $\log N(\mathrm{Mg\,II}) \lesssim 13.8$ occur in a range of $\log N(\mathrm{Mg\,I})/N(\mathrm{Mg\,II})$ values of $-2.2 \lesssim \log N(\mathrm{Mg\,I})/N(\mathrm{Mg\,II}) \lesssim -1.4$. On the other hand, for high column density absorbing components, $\log N(\mathrm{Mg\,II}) \gtrsim 14$, the ratios are lower with a typical $\log N(\mathrm{Mg\,I})/N(\mathrm{Mg\,II}) \sim -2.5$, albeit with larger uncertainties. The range of $N(\mathrm{Mg\,I})/N(\mathrm{Mg\,II})$ in Figure 6 is consistent with what has been found for randomly selected Mg II absorbers by Churchill et al. (2003).

In Zahedy et al. (2016), we performed a series of photoionization calculations for a photoionized gas of tempera-

ture $T = 10^4$ K and a range of gas densities, metallicities, and N(H I). A plane-parallel geometry was assumed for the gas, which was illuminated on both sides with the updated Haardt & Madau (2001) ionizing background radiation field (HM05 in Cloudy v.13.03; Ferland et al. 2013) at $z = 0.5$. For each model, the expected relative abundance ratio between Mg^0 and Mg^+ ions and the ionization fraction ratio between Fe^+ and Mg^+ were calculated for a gas that follows the solar abundance pattern. For absorption components with $\log N(\mathrm{Mg\,II}) \lesssim 13.8$ in the present study, comparing the observed $N(\mathrm{Mg\,I})/N(\mathrm{Mg\,II})$ and predictions from Zahedy et al. (2016) leads to constraints on the gas density of $3 \times 10^{-2}\,\mathrm{cm^{-3}} \lesssim n_\mathrm{H} \lesssim 2 \times 10^{-3}\,\mathrm{cm^{-3}}$. Over the range of allowed gas densities, we find that the ionization fraction of Fe^+ ($f_{\mathrm{Fe^+}}$) remains roughly equal to that of Mg^+ ($f_{\mathrm{Mg^+}}$) in the optically-thick regime and lower than Mg^+ in optically-thin gas. As a result, $f_{\mathrm{Fe^+}}/f_{\mathrm{Mg^+}} < 1$ and $N(\mathrm{Fe\,II})/N(\mathrm{Mg\,II})$, which is equal to $(f_{\mathrm{Fe^+}}/f_{\mathrm{Mg^+}}) \times N(\mathrm{Fe})/N(\mathrm{Mg})$, marks a lower limit to the underlying $N(\mathrm{Fe})/N(\mathrm{Mg})$.

For strong Mg II components of $\log N(\mathrm{Mg\,II}) \gtrsim 14$, however, the observed low $N(\mathrm{Mg\,I})/N(\mathrm{Mg\,II})$ ratios require a low density gas of $n_\mathrm{H} \approx 10^{-3}\,\mathrm{cm^{-3}}$ for the same HM05 ionizing radiation intensity. The inferred low gas density together with a large $N(\mathrm{Mg\,II})$ implies a cloud size of > 10 kpc if the gas has a solar metallicity or > 100 kpc if the gas metallicity is 0.1 solar. The unphysically large cloud sizes inferred for the strongest Mg II absorbing components raise questions for the accuracy of the photoionization models.

Because the observed ionic ratios in photoionization models is dictated by the ionization parameter, which is the number of ionizing photons per atom, a natural explanation for the inferred low gas density is that the ionizing radiation intensity has been underestimated. To increase the ionizing radiation intensity from the standard HM05, we experiment with adding a local ionizing radiation field due to the absorbing galaxy. We first generate a synthetic galaxy spectrum using Starburst99 (Leitherer et al. 1999) and assuming a star formation rate of 1 $M_\odot\,\mathrm{yr^{-1}}$, an age of 10^7 yr, and an ionizing photon escape fraction of 2%. Then, we normalize the flux to match an L_* galaxy at $z = 0.5$. For a gas cloud located at 15 kpc from the galaxy, we find that the ionizing radiation from the galaxy provides a 20-fold increase to the number density of hydrogen-ionizing photons. With an increased ionizing radiation intensity, the inferred underlying gas density increases accordingly. We find that with this revised radiation field the observed low $N(\mathrm{Mg\,I})/N(\mathrm{Mg\,II})$ for strong Mg II components of $\log N(\mathrm{Mg\,II}) \gtrsim 14$ can be reproduced for a gas density of $n_\mathrm{H} \sim 0.01\,\mathrm{cm^{-3}}$. At this gas density, we find that $\log f_{\mathrm{Fe^+}}/f_{\mathrm{Mg^+}} \approx -0.4$ and confirm that the observed $N(\mathrm{Fe\,II})/N(\mathrm{Mg\,II})$ represents a lower limit to the underlying $N(\mathrm{Fe})/N(\mathrm{Mg})$.

An alternative explanation for the observed low $N(\mathrm{Mg\,I})/N(\mathrm{Mg\,II})$ in strong Mg II absorbing components is the presence of additional heating sources that may increase the ionization of the gas in a warmer temperature regime. To explore this alternative scenario, we repeat the photoionization calculations for a higher temperature of $T = 3 \times 10^4$ K, assuming the original HM05 radiation field. The adopted higher temperature is motivated by the observed Doppler parameters of individual Mg II, Mg I and Fe II absorption components. A median value of $b \sim 5$ km s^{-1} is found for each of the three transitions, placing an upper limit on the allowed gas temperature at $T \lesssim 3 \times 10^4$ K.

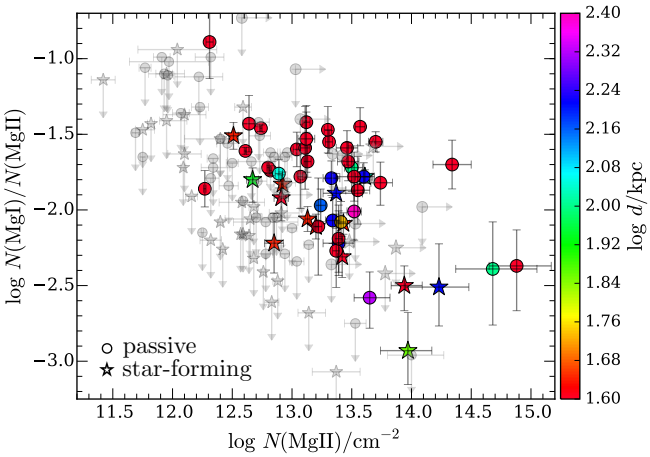

Figure 6. Observed Mg I to Mg II column density ratio, $N(\mathrm{Mg\,I})/N(\mathrm{Mg\,II})$, versus Mg II column density, $N(\mathrm{Mg\,II})$, for individual components identified in our Voigt profile analysis (§ 3). Absorption components associated with passive galaxies are plotted in circle symbols, whereas those associated with star-forming galaxies are plotted in star symbols. The error bars associated with each data point show the measurement uncertainties. The color of each data point represents the projected distance d of the absorbing galaxy to the background QSO sightline. When a Mg II absorbing component has no corresponding Mg I absorption detected, it is shown as a downward arrow, with the gray data point indicating the 2-σ upper limit of $N(\mathrm{Mg\,I})/N(\mathrm{Mg\,II})$.

The resulting model predictions show that the observed $\log N(\mathrm{Mg\,I})/N(\mathrm{Mg\,II}) \sim -2.5$ in most $\log N(\mathrm{Mg\,II}) \gtrsim 14$ absorbing components can also be reproduced for a warm ($T = 3 \times 10^4$ K) optically-thick gas of $\log N(\mathrm{H\,I}) \gtrsim 19$ and 0.1 solar metallicity under a standard HM05 radiation field over a wide range of gas densities. For gas with lower-N(H I), a still higher gas temperature is required, which then becomes incompatible with the observed b value. Imposing a maximum cloud size of $l \sim 10$ kpc based on observations of Galactic high-velocity clouds (e.g., Putman et al. 2012) constrains the gas density to be $n_\mathrm{H} \gtrsim 4 \times 10^{-3}\,\mathrm{cm^{-3}}$ for a gas with 0.1 solar metallicity. Over the range of allowed n_H, $\log f_{\mathrm{Fe^+}}/f_{\mathrm{Mg^+}} \approx -0.3$, indicating that the observed $N(\mathrm{Fe\,II})/N(\mathrm{Mg\,II})$ marks a lower limit to the underlying $N(\mathrm{Fe})/N(\mathrm{Mg})$.

In summary, the exercise described in this section demonstrates that *for both weak and strong Mg II absorption systems identified in this study, the observed* $N(\mathrm{Fe\,II})/N(\mathrm{Mg\,II})$ *ratio represents a lower limit to the underlying elemental* (Fe/Mg) *ratio of the gas for both optically-thin and thick gases.* Comparing the observed $N(\mathrm{Fe\,II})/N(\mathrm{Mg\,II})$ to the solar (Fe/Mg) abundance ratio from Asplund et al. (2009; dotted line in Figures 3 − 5), our analysis shows that $> 60\%$ of passive galaxies exhibit an enhanced Fe/α elemental abundance ratio at $d \lesssim 60$ kpc that exceeds what is observed in the solar neighborhood. At the same time, the majority of passive galaxies at $d \gtrsim 100$ kpc and all star-forming galaxies at $d \lesssim 150$ kpc exhibit chemical compositions consistent with α-element enhancement.

5.2 Differential dust depletion

It is known from observations of the Milky Way ISM that Fe is more readily incorporated into dust grains than Mg, showing in excess of 0.5 dex more depletion than Mg in cool ($T \sim 500$ K) ISM gas (e.g, Savage & Sembach 1996). Including such differential dust depletion, the inferred $N(\mathrm{Fe})/N(\mathrm{Mg})$ after accounting for possible differential ionization fraction correction may still represent a lower limit to the underlying elemental abundance ratio. At the same time, dust grains are expected to be easily destroyed in warmer environment (e.g., Draine & Salpeter 1979). Indeed, the observed differential depletion between Fe and Mg reduces to ≈ 0.35 dex in warm ($T \approx 6000$ K) ISM gas (e.g, Savage & Sembach 1996). For Mg II absorbing gas of $T \sim 10^4$ K, it is expected that dust destruction is still more effective (e.g., McKee et al. 1987) and that differential dust depletion is at its minimum. X-ray observations of the hot ISM gas in 19 local early-type galaxies from Humphrey & Buote (2006) have yielded a median Fe to Mg ratio of $\log(\mathrm{Fe/Mg}) = -0.01 \pm 0.18$ at $d \lesssim 10-60$ kpc from these galaxies. This median value is consistent with what we found for singly ionized Fe and Mg at $d < 60$ kpc from $z \sim 0.5$ passive galaxies, supporting the expectation that dust depletion is not significant in the cool ($T \sim 10^4$ K) halo clouds revealed by Mg II absorption transitions.

However, it is possible that the observed low $N(\mathrm{Fe\,II})/N(\mathrm{Mg\,II})$ ratio around star-forming galaxies is due to a larger amount of differential dust depletion around these galaxies, particularly for the Mg II absorbers detected at $d < 50$ kpc. These absorbers are all relatively strong with $W_r(2796) \gtrsim 0.6$ Å, and it has been shown that $\approx 30-40\%$ of these strong Mg II absorbers contain neutral gas of $N(\mathrm{H\,I}) \gtrsim 2\times10^{20}\mathrm{cm}^{-2}$ (e.g., Rao et al. 2006). Therefore, a large fraction of these absorbers are likely to arise in DLA gas. For DLAs at $z \sim 0.5-3$, Fe is found to be more depleted than Mg by ≈ 0.2 dex (e.g., Vladilo et al. 2011; De Cia et al. 2016). If dust is present in these strong Mg II absorbers around $z \sim 0.5$ star-forming galaxies, then adopting the mean differential dust depletion between Fe and Mg observed for DLAs would imply a median underlying (Fe/Mg) abundance ratio of $\log(\mathrm{Fe/Mg}) = -0.05$ at $d < 50$ kpc, comparable to both the solar value and what is observed at $d < 60$ kpc from passive galaxies. For weaker Mg II absorbers at $d > 50$ kpc, the dust content is expected to be significantly less and little correction for differential dust depletion is expected.

The differential dust depletion between Fe and Mg can be inferred directly for the absorption systems around two star-forming galaxies in the $d < 50$ kpc subsample, providing a comparison to the underlying (Fe/Mg) ratio implied from the subsample median. For the star-forming galaxy at $z = 0.101$ and $d = 8$ kpc from PKS 0439−433, the roughly solar metallicity known for the DLA gas associated with this galaxy (Chen et al. 2005; Som et al. 2015) allows us to estimate the dust depletion factors for Fe and Mg based on a known correlation between dust depletion and gas-phase metallicity. The differential dust depletion between Fe and Mg is expected to vary between +0.5 and +0.8 dex for a solar-metallicity gas, based on observations of Galactic absorbers (e.g., De Cia et al. 2016). If dust is present in this DLA, this range of differential dust depletion would imply an underlying (Fe/Mg) abundance ratio of $\log(\mathrm{Fe/Mg}) = -0.1$ to +0.2 for the gas. Similarly for the ultra-strong Mg II absorber associated with the $z = 1.24$ galaxy at $d = 17$ kpc from SDSSJ 1430+0149, although the metallicity is not known, the relative abundance ratio of Cr to Zn is estimated to be $[\mathrm{Cr/Zn}] = -0.51 \pm 0.06$ (Zych et al. 2009), indicating a modest level of dust depletion comparable to what is seen in the Galactic Halo (e.g., Savage & Sembach 1996). The expected differential depletion between Fe and Mg in such an environment is $\approx +0.2$ dex, which would imply an underlying (Fe/Mg) ratio of $\log(\mathrm{Fe/Mg}) = -0.05$ for this Mg II absorber. In both of these cases, applying the estimated dust depletion correction individually for each galaxy results in an implied underlying (Fe/Mg) abundance ratio that is comparable to solar value, consistent with what is found by applying the mean dust depletion correction for DLAs on the median value for the inner-d bin. This exercise lends strong support for the finding that solar-level (Fe/Mg) gas may not be uncommon at $d < 50$ kpc from intermediate-redshift, star-forming galaxies.

5.3 Implications on the origin of chemically enriched gas in galaxy halos

As previously mentioned in § 1, iron is produced in both core collapse and Type Ia SNe, whereas magnesium is produced primarily in massive stars and core-collapse SNe. Specifically, a Type Ia supernova is expected to produce $\sim 0.7\,M_\odot$ of Fe while releasing no more than $0.02\,M_\odot$ of magnesium at the same time (e.g., Iwamoto et al. 1999). Different types of SNe originate in different progenitor stars of different stellar ages. The elemental (Fe/Mg) ratio therefore provides a measure of the relative contributions from different massive stars to the chemical enrichment history of a galaxy (e.g., de Plaa et al. 2007; Zahedy et al. 2016). Consequently, the inferred lower limit of the underlying (Fe/Mg) elemental abundance ratio from the observed $N(\mathrm{Mg\,I})/N(\mathrm{Mg\,II})$ provides a useful "clock" for timing the age of the stellar population. In addition, the spatial profiles of $N(\mathrm{Mg\,I})/N(\mathrm{Mg\,II})$ offers important constraints for the extent of SNe Ia-dominated chemical enrichment in galactic halos.

For quiescent galaxies in this study, the observed $N(\mathrm{Fe\,II})/N(\mathrm{Mg\,II})$ at $d \lesssim 60$ kpc is high with a median and dispersion of $\log\langle N(\mathrm{Fe\,II})/N(\mathrm{Mg\,II})\rangle_{\mathrm{med}} = -0.06 \pm 0.15$. The large column density ratio implies a lower limit to the underlying (Fe/Mg) ratio of the gas at $[\mathrm{Fe/Mg}] \equiv \log(\mathrm{Fe/Mg}) - \log(\mathrm{Fe/Mg})_\odot \gtrsim 0$. The implied fractional contribution from SNe Ia to the chemical enrichment of the gas is $f_{\mathrm{Ia}} \gtrsim 17\%$ based on the expected nucleosynthetic yields for Type Ia and core-collapse SNe from Iwamoto et al. (1999). This minimum value is comparable to what has been estimated for solar-abundance gas in the Milky Way (e.g., Tsujimoto et al. 1995). With such a significant contribution from SNe Ia, it can also be expected that cool gas at $d \lesssim 60$ kpc from passive galaxies has been enriched to a relatively high metallicity, reflecting the role of multiple generations of massive stars and SNe Ia in its chemical enrichment history. Indeed, this expectation is at least consistent with what has been found in the hot ISM of local elliptical galaxies, where near-solar mean metallicities are commonly observed at a similar range of d (e.g., Humphrey & Buote 2006; Loewen-

stein & Davis 2010, 2012). Furthermore, we note that Fe/α radial profile measurements are available from X-ray observations of the hot ISM in several nearby massive quiescent galaxies (e.g, Nagino & Matsushita 2010; Loewenstein & Davis 2010, 2012), where it has been found that the Fe/α radial profile in these galaxies is consistent within measurement errors with being flat at [Fe/α] ~ 0 level at $d \lesssim 40$ kpc, comparable to what can be inferred from our observations at $d \lesssim 60$ kpc from $z \sim 0.5$ passive galaxies.

Our analysis also provides a quantitative constraint on the Fe/α ratio at $d \gtrsim 100$ kpc from passive galaxies, where the gas is typically too diffuse to be detected in emission even in the local universe. We find that at $d \gtrsim 100$ kpc the absorbing gas generally shows lower $N(\mathrm{Fe\,II})/N(\mathrm{Mg\,II})$ ratios than typically seen at $d \lesssim 60$ kpc. Specifically for passive galaxies, the $N(\mathrm{Fe\,II})/N(\mathrm{Mg\,II})$ ratios at $d \gtrsim 100$ kpc can be characterized by a 85% upper limit to the underlying distribution of $\log \langle N(\mathrm{Fe\,II})/N(\mathrm{Mg\,II})\rangle_{\rm med} < -0.3$. In at least three out of seven cases ($\approx 40\%$), the absorbing gas displays $\log \langle N(\mathrm{Fe\,II})/N(\mathrm{Mg\,II})\rangle_{\rm med} \lesssim -0.6$. Allowing a modest differential ionization fraction between Fe^+ and Mg^+ of up to $\log f_{\rm Fe^+}/f_{\rm Mg^+} \approx -0.3$ dex (assuming an optically thick gas, see § 5.2), the implied underlying (Fe/Mg) relative abundance ratio is [Fe/Mg] $\lesssim -0.2$ for a $\log N(\mathrm{Fe\,II})/N(\mathrm{Mg\,II}) = -0.6$ gas. This range of [Fe/Mg] ratios is comparable to that of high-redshift DLAs, where the mean [Fe/α] has been found to be -0.26 ± 0.12 at $z \gtrsim 3$ (e.g., Rafelski et al. 2012). For [Fe/Mg] $\lesssim -0.2$, the expected maximum fractional contribution from SNe Ia to the chemical enrichment is $f_{\rm Ia} \lesssim 5\%$, based on supernova nucleosynthetic yields from Iwamoto et al. (1999). Our analysis therefore indicates that SNe Ia-driven chemical enrichment is relatively localized in inner halos at $d \lesssim 60$ kpc and that the chemical enrichment of the cool gas at $d \gtrsim 100$ kpc from $z = 0.5$ passive galaxies is consistent with an early enrichment driven by core-collapse SNe.

For star-forming galaxies, interpretations of our observations are more uncertain. As previously noted in § 5.2, if differential dust depletion is important, then the absorbing gas at $d \lesssim 50$ kpc from these star-forming galaxies may also have a near solar-level (Fe/Mg) ratio. Such a high level Fe/Mg ratio may not be surprising for a mature disk galaxy at low- to intermediate-redshifts. However, it is interesting to find that a strong Mg II absorber of $W_r(2796) = 2.86$ at $d = 17$ kpc from a star-forming galaxy at $z = 1.24$ could potentially have a solar Fe/Mg ratio after differential dust depletion corrections. The implication is that the galaxy contains a relatively evolved stellar population, while maintaining an active level of star formation when the universe was ≈ 5 Gyr old. Follow-up studies of the stellar populations and star formation history in this galaxy are necessary for a better understanding of the observed high Fe/Mg ratio in the absorber.

At $d > 70$ kpc from star-forming galaxies, the observed Fe II to Mg II column density ratios are generally low with a median and dispersion of $\log \langle N(\mathrm{Fe\,II})/N(\mathrm{Mg\,II})\rangle_{\rm med} = -0.91 \pm 0.44$. For a median $N(\mathrm{Mg\,I})/N(\mathrm{Mg\,II})$ ratio of $\log N(\mathrm{Mg\,I})/N(\mathrm{Mg\,II}) = -1.9$, the expected differential ionization fraction between Fe^+ and Mg^+ is $\log f_{\rm Fe^+}/f_{\rm Mg^+} \approx -0.6$ dex for an optically-thin gas (and negligible for an optically-thick gas). Applying this ionization correction leads to an implied underlying (Fe/Mg) relative abundance ratio of [Fe/Mg] $\lesssim -0.2$ at $d = 70 - 160$ kpc. Similar to what is seen at $d > 100$ kpc from passive galaxies, cool gas at $d > 70$ kpc from star-forming galaxies also shows an α-element enhanced abundance pattern driven by core-collapse SNe.

In summary, our analysis suggests that Fe/α in galactic halos declines with increasing projected distance from both passive and star-forming galaxies. At $d \lesssim 60$ kpc, a significant contribution from SNe Ia ($f_{\rm Ia} \gtrsim 15\%$) is necessary to explain the observed Fe/Mg ratios, whereas at $d \gtrsim 70$ kpc, contributions from SNe Ia are limited to $f_{\rm Ia} \lesssim 5\%$ in both star-forming and quiescent halos. Together, our analysis shows that SNe Ia-driven chemical enrichment is relatively localized in inner halos at $d \lesssim 60$ kpc. Alternatively, inflowing gas from the IGM could also "dilute" an Fe-rich gas and produce a declining Fe/α radial profile in the halo, because accreted IGM gas is expected to show an α-enhanced abundance pattern which reflects the early enrichment history (e.g., Rauch et al. 1997). However, such dilution effect is likely minimal if the metallicity of an α-enhanced inflowing gas is significantly lower than the Fe-rich gas.

It is clear that there is a significant scatter in the empirical measurements of $N(\mathrm{Fe\,II})/N(\mathrm{Mg\,II})$, while the inferred $f_{\rm Ia}$ depends sensitively on the input Fe/α elemental abundance ratio. We anticipate that future observations combining metallicity and relative abundance measurements in stars/ISM and in halo gas for a large sample of galaxies will provide the precision necessary to distinguish between different scenarios.

ACKNOWLEDGMENTS

We thank the anonymous referee for thoughtful comments which helped us improve the paper. The authors thank Sean Johnson and John Mulchaey for useful discussions and suggestions, and Yun-Hsin Huang, and Sean Johnson for obtaining some of the MIKE spectra analyzed here. This work is based on data gathered with the 6.5 m Magellan Telescopes located at Las Campanas Observatory, the ESO telescopes at the La Silla Paranal Observatory, and the NASA/ESA Hubble Space Telescope operated by the Space Telescope Science Institute and the Association of Universities for Research in Astronomy, Inc., under NASA contract NAS 5-26555. Additional data were obtained at the W.M. Keck Observatory, which is operated as a scientific partnership among the California Institute of Technology, the University of California and the National Aeronautics and Space Administration. The Observatory was made possible by the generous financial support of the W.M. Keck Foundation.

REFERENCES

Agertz, O., Teyssier, R., & Moore, B. 2009, MNRAS, 397, L64

Asplund, M., Grevesse, N., Sauval, A. J., & Scott, P. 2009, ARA&A, 47, 481

Bernstein, R., Shectman, S. A., Gunnels, S. M., Mochnacki, S., & Athey, A. E. 2003, Proc. SPIE, 4841, 1694

Booth, C. M., Agertz, O., Kravtsov, A. V., & Gnedin, N. Y. 2013, ApJ, 777, L16
Borthakur, S., Heckman, T., Strickland, D., Wild, V., & Schiminovich, D. 2013, ApJ, 768, 18
Chen, H.-W., Lanzetta, K. M., Webb, J. K., & Barcons, X. 1998, ApJ, 498, 77
Chen, H.-W., Lanzetta, K. M., Webb, J. K., & Barcons, X. 2001, ApJ, 559, 654
Chen, H.-W., Kennicutt, R. C., Jr., & Rauch, M. 2005, ApJ, 620, 703
Chen, H.-W., Helsby, J. E., Gauthier, J.-R., et al. 2010, ApJ, 714, 1521
Churchill, C. W., Steidel, C. C., & Vogt, S. S. 1996, ApJ, 471, 164
Churchill, C. W., Mellon, R. R., Charlton, J. C., et al. 2000, ApJS, 130, 91
Churchill, C. W., & Vogt, S. S. 2001, AJ, 122, 679
Churchill, C. W., Vogt, S. S., & Charlton, J. C. 2003, AJ, 125, 98
Conroy, C., van Dokkum, P. G., & Kravtsov, A. 2015, ApJ, 803, 77
Dawson, K. S., Schlegel, D. J., Ahn, C. P., et al. 2013, AJ, 145, 10
De Cia, A., Ledoux, C., Mattsson, L., et al. 2016, arXiv:1608.08621
de Plaa, J., Werner, N., Bleeker, J. A. M., et al. 2007, A&A, 465, 345
Dessauges-Zavadsky, M., Prochaska, J. X., D'Odorico, S., Calura, F., & Matteucci, F. 2006, A&A, 445, 93
D'Odorico, S., Cristiani, S., Dekker, H., et al. 2000, Proc. SPIE, 4005, 121
Ellingson, E., Green, R. F., & Yee, H. K. C. 1991, ApJ, 378, 476
Faber, S. M., Willmer, C. N. A., Wolf, C., et al. 2007, ApJ, 665, 265
Ferland, G. J., Porter, R. L., van Hoof, P. A. M., et al. 2013, Rev. Mexicana Astron. Astrofis., 49, 137
Förster, F., & Schawinski, K. 2008, MNRAS, 388, L74
Gauthier, J.-R., Chen, H.-W., & Tinker, J. L. 2009, ApJ, 702, 50
Gauthier, J.-R., Chen, H.-W., & Tinker, J. L. 2010, ApJ, 716, 1263
Gauthier, J.-R., & Chen, H.-W. 2011, MNRAS, 418, 2730
Gauthier, J.-R. 2013, MNRAS, 432, 1444
Green J. C., Froning C. S., Osterman S. et al. 2012, ApJ, 744, 60
Guillemin, P., & Bergeron, J. 1997, A&A, 328, 499
Haardt, F., & Madau, P. 2001, Clusters of Galaxies and the High Redshift Universe Observed in X-rays, 64
Huang, Y.-H., Chen, H.-W., Johnson, S. D., Weiner, B. J. 2016, MNRAS, 455, 1713
Humphrey, P. J., & Buote, D. A. 2006, ApJ, 639, 136
Iwamoto, K., Brachwitz, F., Nomoto, K., et al. 1999, ApJS, 125, 439
Leitherer, C., Schaerer, D., Goldader, J. D., et al. 1999, ApJS, 123, 3
Lehner, N., Howk, J. C., Tripp, T. M., et al. 2013, ApJ, 770, 138
Lidman, C., Courbin, F., Kneib, J.-P., et al. 2000, A&A, 364, L62
Loewenstein, M., & Davis, D. S. 2010, ApJ, 716, 384
Loewenstein, M., & Davis, D. S. 2012, ApJ, 757, 121
Muzahid, S., Kacprzak, G. G., Churchill, C. W., et al. 2015, ApJ, 811, 132
Kacprzak, G. G., Churchill, C. W., Ceverino, D., et al. 2010, ApJ, 711, 533
Kacprzak, G. G., Churchill, C. W., Evans, J. L., Murphy, M. T., & Steidel, C. C. 2011, MNRAS, 416, 3118
Murray, N., Ménard, B., & Thompson, T. A. 2011, ApJ, 735, 66
Nagino, R., & Matsushita, K. 2010, PASJ, 62, 787
Narayanan, A., Charlton, J. C., Misawa, T., Green, R. E., & Kim, T.-S. 2008, ApJ, 689, 782-815
Nielsen, N. M., Churchill, C. W., & Kacprzak, G. G. 2013, ApJ, 776, 115
Nomoto K., Tominaga N., Umeda H., Kobayashi C., Maeda K., 2006, Nucl. Phys. A, 777, 424
Nomoto, K., Kobayashi, C., & Tominaga, N. 2013, ARA&A, 51, 457
Putman, M. E., Peek, J. E. G., & Joung, M. R. 2012, ARA&A, 50, 491
Rafelski, M., Wolfe, A. M., Prochaska, J. X., Neeleman, M., & Mendez, A. J. 2012, ApJ, 755, 89
Rao, S. M., Turnshek, D. A., & Nestor, D. B. 2006, ApJ, 636, 610
Rauch, M., Haehnelt, M.G., Steinmetz, M., 1997, ApJ, 481, 601
Rigby, J. R., Charlton, J. C., & Churchill, C. W. 2002, ApJ, 565, 743
Savage, B. D., & Sembach, K. R. 1996, ARA&A, 34, 279
Serra, P., Oosterloo, T., Morganti, R., et al. 2012, MNRAS, 422, 1835
Som, D., Kulkarni, V. P., Meiring, J., et al. 2015, ApJ, 806, 25
Steidel, C. C., Dickinson, M., Meyer, D. M., Adelberger, K. L., & Sembach, K. R. 1997, ApJ, 480, 568
Steidel, C. C., Kollmeier, J. A., Shapley, A. E., et al. 2002, ApJ, 570, 526
Tsujimoto, T., Nomoto, K., Yoshii, Y., et al. 1995, MNRAS, 277, 945
Vladilo, G., Abate, C., Yin, J., Cescutti, G., & Matteucci, F. 2011, A&A, 530, A33
Vogt, S. S., Allen, S. L., Bigelow, B. C., et al. 1994, Proc. SPIE, 2198, 362
Wang, B. 1993, ApJ, 415, 174
Young, L. M., Bureau, M., Davis, T. A., et al. 2011, MNRAS, 414, 940
Zahedy, F. S., Chen, H.-W., Rauch, M., Wilson, M. L., & Zabludoff, A. 2016, MNRAS, 458, 2423
Zhu, G., Ménard, B., Bizyaev, D., et al. 2014, MNRAS, 439, 3139
Zych, B. J., Murphy, M. T., Hewett, P. C., & Prochaska, J. X. 2009, MNRAS, 392, 1429

This paper has been typeset from a TEX/LATEX file prepared by the author.